Computational modeling of chemo-bio-mechanical coupling: A systems-biology approach towards wound healing

Adrián Buganza Tepole[a], Ellen Kuhl[b,*]

[a]*Department of Mechanical Engineering, Stanford University, Stanford, CA 94305, USA*
[b]*Departments of Mechanical Engineering, Bioengineering, and Cardiothoracic Surgery, Stanford University, Stanford, CA 94305, USA*

Abstract

Hypertrophic scarring is the result of excessive collagen deposition during wound healing. Wound healing is a well-synchronized cascade of chemical, biological, and mechanical events that act in concert to restore the damaged tissue. An imbalance between these events can lead to an abnormal response in the form of thick, stiff, and sometimes painful scar. Despite intense efforts to decipher the signaling mechanisms of wound healing, the role of mechanics remains severely understudied and poorly understood. Here we establish a computational systems biology model to identify the chemical, biological, and mechanical mechanisms of scar formation. Our approach is unconditionally stable, geometrically flexible, and conceptually modular. To ensure unconditional stability, we employ an implicit backward Euler scheme in time. To enable geometrical flexibility, we use a finite element discretization in space. To maintain modularity, we first introduce a generic framework for arbitrary chemical, biological, and mechanical fields. Then, we introduce the model problem of wound healing in terms of a particular chemical signal, inflammation, a particular biological cell type, fibroblasts, and a particular mechanical model, isotropic hyperelasticity. To explore the cross-talk between the individual fields, we perform systematic sensitivity analyses both in time and space. Altogether, our model is a decisive step towards the incorporation of individualized data in wound healing. Driven by the increasing importance of systems medicine and translational systems biology, our formulation has the potential to significantly improve effective wound management and optimize treatment options on an individualized patient-specific basis.

1. Motivation

Effective wound management is a quotidian concern in clinical practice, since abnormal wound healing can initiate hypertrophic scars associated with serious sequelae from deteriorated skin characteristics to psychological trauma [2]. The health care cost related to wound treatment is jolting; wounds are common to many clinical procedures and span all patient demographics [3]. Fostering a healthy tissue response is a non-trivial task. The process of wound healing is a complex sequence of interrelated events that involve mechanical cues, coordinated cell behavior, and the interaction of numerous chemical signals [10]. In such a scenario, planning effective healing on a patient-specific basis becomes almost impossible. Computational systems biology has found a niche to enrich our understanding of this complex problem [21]. However, despite intense efforts to characterize the healing process with mathematical models, simulation of wound healing in arbitrary three-dimensional geometries remains an open problem.

Disrupting the integrity of skin triggers a cascade of events that are common to all inflammation-based systems in the human body [53]. Additionally, during dermal wound healing, specialized processes take place to restitute the particular functional requirements of dermal tissue [13]. Perhaps the most distinct feature of this system is the interaction of different key players across scales, both in space and time. During the past decades, scientists have successfully identified and characterized the individual aspects of this network, but a holistic understanding of the healing process as a whole remains obscure [54].

1.1. Wound healing across the spatial scales

The spatial scales of interest for the healing system range from the order of micrometers, to millimeters, centimeters, and decimeters [6]. Figure 1 illustrates the multi-scale nature of the healing process with four interacting spatial scales [36]: the system level, the organ level, the tissue level, and the cell level [17].

On the cell level, the smallest spatial scale of the order of micrometers, single cells are the individual actors, which directly affect the healing process [44]. In the damaged dermal tissue and its surroundings, the following cell types are present: two types of leukocytes, neutrophils and macrophages, dispose pathogens and debris and establish gradients of growth factors; endothelial cells generate a new vasculature; keratinocytes divide and migrate across the epidermis to produce a new protective outermost layer; and fibroblasts deposit collagen and generate active stresses to contract the wound [32, 52].

On the tissue level, the next larger scale of the order of millimeters, the actions of the individual cells are smeared out by meso-scale patterns, which emanate from the collective cell behavior. This collective response exhibits distinctive character-

*Correspondence to: Ellen Kuhl, Department of Mechanical Engineering, Stanford University, Stanford, CA 94305, USA, ekuhl@stanford.edu, http://biomechanics.stanford.edu

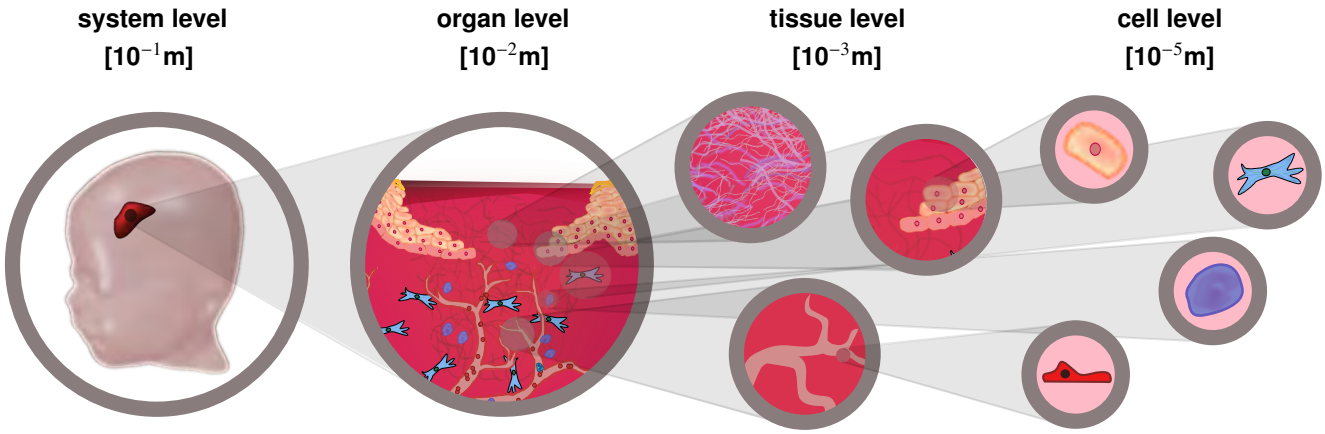

Figure 1: Wound healing across the spatial scales. The chemo-bio-mechanical problem of wound healing spans from the cellular level via the tissue level and organ level to the system level bridging four orders of magnitude in space.

istics, which can no be extrapolated directly from single cell actions. Populations of keratinocyte generate a well-organized traveling wave inwards, and populations of endothelial cells keep strong cell-cell interactions to create fractal-like vascular networks [26, 35]. From this scale upward, both the mechanical response and the reaction-diffusion response of the chemical species can be characterized through field variables using a continuum approach [11, 25].

On the organ level, the scale of the order of centimeters, we can explore the interaction of the mechanical properties, different cell populations, and reaction-diffusion systems of chemical concentrations. The organ level provides a holistic approach to study the role of the individual key players of wound healing, and allows us to explore tissue function in health and disease.

On the system level, the scale of the order of decimeters, we can study the entire system created by the interplay of different organs. Ideally, system level models are generated on a patient-specific basis from individual clinical imaging data [60].

1.2. Wound healing across the temporal scales

The temporal scales of interest for the healing system range from the order of minutes, to hours, days, and weeks [6]. Figure 2 illustrates the multi-scale nature of the healing process with four overlapping temporal scales: hemostasis, inflammation, proliferation, and remodeling [27]. Immediately after the injury occurs, healing is critical to restitute the barrier function of skin. Unfortunately, the initially generated temporary scaffold has only poor mechanical characteristics. Accordingly, subsequent stages of the healing process gradually reconstruct the tissue to ultimately restore the constitution of the uninjured skin [30]. The entire healing process can last for weeks or even months.

During hemostasis, within the order of minutes, the injured region fills with blood, which quickly coagulates. This results in the formation of an emergency scaffold of fibrin fibers. The only cells present in the clot are platelets, responsible for coagulation and the release of growth factors. At the end of this stage, degranulation of the platelets floods the injured site with chemicals to attract leukocytes.

During inflammation, within the order of hours, the first population of leukocytes, neutrophils, arrive at the wound site. Neutrophils remove pathogens and dispose of tissue debris from the injury. Shortly after, a second population of leukocytes, macrophages, migrate into the wound and continue the cleaning process. In addition, they establish gradients of various chemical signals to attract other cell populations [48]. After one or two days, the inflammatory phase smoothly blends into the proliferative phase.

During proliferation, within the order of days, the chemical signaling established by the macrophages attracts specialized cell populations that reconstruct skin. Endothelial cells generate a new vasculature that provides nutrients to the other cell populations [14]. Keratinocytes reconstruct the outermost protective layer, the epidermis, in a process called re-epithelialization [43]. Fibroblasts replace the temporary fibrin scaffold with a collagenous matrix that restitutes the desired mechanical properties of the healed tissue [7]. Although the proliferation phase creates a somewhat functional tissue, the mechanical properties of the newly reconstructed skin are not nearly identical to healthy, uninjured skin: The newly generated material is stiff scar tissue, which is partly provisional and will be replaced during the final remodeling phase [50].

During remodeling, within the order of weeks, fibroblasts slowly tear down and deposit collagen until the matrix approaches the structure of healthy tissue. The remodeling phase can continue for months or even years.

1.3. Modeling wound healing

Wound healing has been studied assiduously both experimentally and theoretically. Recent developments in computational systems biology suggest that we cannot gain a complete understanding of wound healing from studying isolated spatial or temporal scales alone [46]. Rather, trends in modeling seem to converge towards assembling the individual building blocks for a holistic model that, once calibrated, can provide new insight into the baseline system [9, 31]. Systematic perturbations of this system allow us to probe different healing scenarios to ultimately link computational tools with personalized models [41].

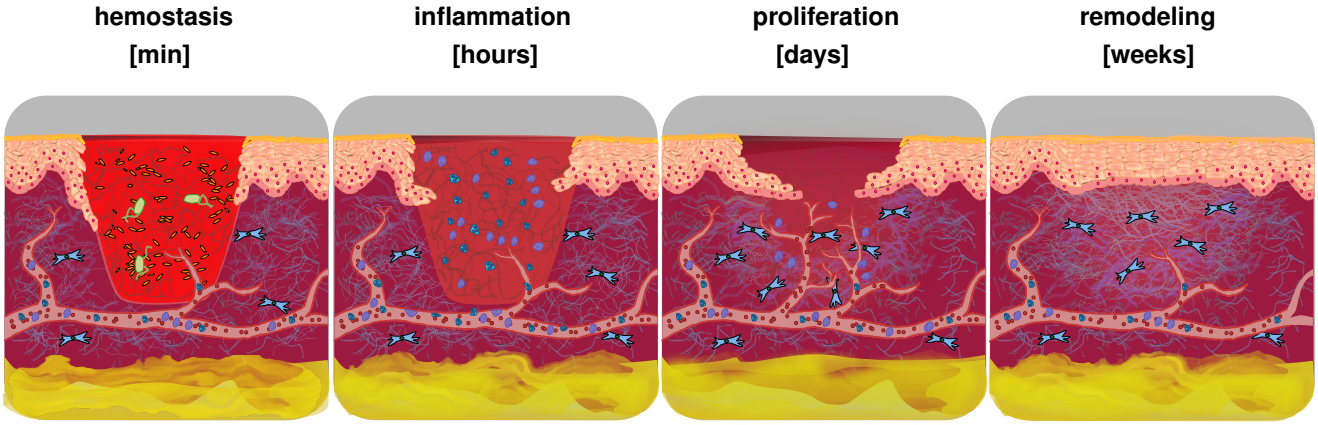

Figure 2: Wound healing across the temporal scales. The chemo-bio-mechanical problem of wound healing spans from the homeostatic phase via the inflammatory phase and proliferative phase to the remodeling phase bridging four orders of magnitude in time.

The first mathematical model of wound healing was introduced in the early 1990s. Its initial goal was to simulate the traveling wave front of growing cell populations at the edge of a wound [42]. Since then, mathematical models have gained in complexity and have gradually incorporated the different components that interact in synchrony to heal the damaged tissue [58]. Recent models can be categorized according to two criteria, the aspect of healing they seek to analyze in detail and the simulation framework employed for the analysis. Three aspects of healing are particularly relevant: re-epithelialization and cell migration; angiogenesis; and mechanical aspects of wound healing such as collagen deposition and wound contraction. Four modeling strategies are prevalent: one-dimensional and axisymmetric continuum models; two-dimensional continuum models; two- and three-dimensional discrete models; and two-dimensional hybrid discrete/continuum models. A recent review article highlights the state of the art in systems biology approaches towards wound healing [6].

Among the different variables that influence the outcome of healing, the importance of mechanical cues has recently been identified with more clarity. Fibroblasts have the capability to sense mechanical signals, to translate them into specific action such as active contraction, and to release chemical substances [55]. We now know that increased stress in the wound site alters fibroblast phenotype by reducing their apoptotic rate and inducing the release of pro-inflammatory signals [1, 33]. In turn, when the inflammation phase is prolonged, fibroblasts divide and migrate into the wound at higher rates, which results in an increased collagen deposition. The ultimate consequence is a poorly structured dermal tissue with thick collagen bundles instead of the smooth, inter-woven collageneous network found in healthy tissue. Visually, the result of such pathological reaction is very clear to the human eye, which can readily recognize hypertrophic scars [57]. However, despite this obvious evidence, only few models have incorporated a detailed mechanical description of the wound environment. While some models have addressed collagen deposition and active wound contraction, their application is limited by the underlying simplified constitutive models for the tissue structure [18, 49]. While such simplifications are adequate for baseline studies and first prototype simulations [22, 23], in the current state, these models are unable to bridge the gap towards arbitrary geometries, large deformations, and complex stress distributions that arise in more realistic settings.

Motivated by the need for a computational framework that incorporates the state-of-the-art development in wound healing, here we present a novel finite element formulation for the chemo-bio-mechanical problem of wound healing in arbitrary geometries. The manuscript is structured as follows: In Section 2, we introduce the generic continuum framework of wound healing. In Section 3, we specify a particular type of the model parameterized in terms of a single chemical signal, a single biological cell density, and the mechanical deformation. In Section 4, we derive the discrete formulation of the particular model problem. In Section 5, we present sensitivity studies and selected examples to showcase the features of the model. Finally, in Section 6, we provide a discussion and a brief outlook.

2. Chemo-bio-mechanical problem

We begin by introducing the generic equations that govern the dynamics of inflammation-based systems. In general, the underlying chemo-bio-mechanical problem can be characterized through three spatially and temporally interacting building blocks: chemical fields including substances such as growth factors and inflammation signals, here summarized in the vector $\mathbf{c}(\boldsymbol{X},t) = [c_1(\boldsymbol{X},t), c_2(\boldsymbol{X},t), ..., c_{n_c}(\boldsymbol{X},t)]^{\mathrm{t}}$; biological fields including cell populations, here summarized in the vector $\boldsymbol{\rho}(\boldsymbol{X},t) = [\rho_1(\boldsymbol{X},t), \rho_2(\boldsymbol{X},t), ..., \rho_{n_\rho}(\boldsymbol{X},t)]^{\mathrm{t}}$; and mechanical fields including the deformation $\boldsymbol{\varphi}(\boldsymbol{X},t)$, which are possibly locally supplemented by microstructural internal variables such as microstructural directions $\mathbf{n}(\boldsymbol{X},t) = [n_1(\boldsymbol{X},t), n_2(\boldsymbol{X},t), ..., n_{n_n}(\boldsymbol{X},t)]^{\mathrm{t}}$ and local concentrations $\mathbf{w}(\boldsymbol{X},t) = [w_1(\boldsymbol{X},t), w_2(\boldsymbol{X},t), ..., w_{n_w}(\boldsymbol{X},t)]^{\mathrm{t}}$. In the following, we characterize the evolution equations of these sets of variables in a continuum setting.

2.1. Chemical problem: Chemical concentrations

Chemically, the evolution of the set of chemical concentrations $\mathbf{c}$ is balanced by the chemical flux $\mathbf{q}^{\mathrm{c}}$ and the chemical source $\mathbf{f}^{\mathrm{c}}$,

$$\dot{\mathbf{c}} = \operatorname{div} \mathbf{q}^{\mathrm{c}}(\nabla \mathbf{c}) + \mathbf{f}^{\mathrm{c}}(\mathbf{c}, \boldsymbol{\rho}) \,, \tag{1}$$

where $\{\dot{\circ}\} = \mathrm{d}\{\circ\} / \mathrm{d}t$ denotes the material time derivative and $\nabla\{\circ\}$ and $\operatorname{div}\{\circ\}$ denote the spatial gradient and divergence. The chemical flux $\mathbf{q}^{\mathrm{c}}$ is typically modeled as a linear function of the gradient of the chemical concentration $\nabla \mathbf{c}$ to indicate that the chemical signal can diffuse freely in the domain of interest,

$$\mathbf{q}^{\mathrm{c}} = \mathbf{D}^{\mathrm{cc}} \cdot \nabla \mathbf{c} \,, \tag{2}$$

where $\mathbf{D}^{\mathrm{cc}}$ denotes the chemical diffusion tensor. The chemical source $\mathbf{f}^{\mathrm{c}}$ typically consists of a production term $\mathbf{f}^{\mathrm{c}}_{\mathrm{p}}$ and a degradation term $\mathbf{f}^{\mathrm{c}}_{\mathrm{d}}$, whereby the degradation typically scales linearly with the concentration $\mathbf{c}$,

$$\mathbf{f}^{\mathrm{c}}(\mathbf{c}, \boldsymbol{\rho}) = \mathbf{f}^{\mathrm{c}}_{\mathrm{p}}(\mathbf{c}, \boldsymbol{\rho}) - \mathbf{f}^{\mathrm{c}}_{\mathrm{d}}(\mathbf{c}, \boldsymbol{\rho})\, \mathbf{c} \,. \tag{3}$$

In general, $\mathbf{f}^{\mathrm{c}}_{\mathrm{p}}$ and degradation $\mathbf{f}^{\mathrm{c}}_{\mathrm{d}}$ can be functions of all chemical concentrations $\mathbf{c}$ and all cell populations $\boldsymbol{\rho}$. They contain the information about how chemical substances are produced and degraded through chemical reactions with other chemical substances and by the different biological cells. In homeostasis, in the absence of chemical gradients $\nabla \mathbf{c} = \mathbf{0}$, the chemical production and degradation balance each other, $\mathbf{f}^{\mathrm{c}}_{\mathrm{p}} = \mathbf{f}^{\mathrm{c}}_{\mathrm{d}} \mathbf{c}$.

2.2. Biological problem: Biological cell densities

Biologically, the evolution of the set of cell densities $\boldsymbol{\rho}$ is balanced by the biological flux $\mathbf{q}^{\rho}$ and the biological source $\mathbf{f}^{\rho}$,

$$\dot{\boldsymbol{\rho}} = \operatorname{div} \mathbf{q}^{\rho}(\mathbf{c}, \nabla \mathbf{c}, \boldsymbol{\rho}, \nabla \boldsymbol{\rho}) + \mathbf{f}^{\rho}(\mathbf{c}, \boldsymbol{\rho}, \nabla \boldsymbol{\varphi}) \,. \tag{4}$$

The biological flux $\mathbf{q}^{\rho}$ typically consists of two contributions,

$$\mathbf{q}^{\rho} = \mathbf{D}^{\rho\rho} \cdot \nabla \boldsymbol{\rho} + \mathbf{D}^{\rho\mathrm{c}}(\mathbf{c}, \boldsymbol{\rho}) \cdot \nabla \mathbf{c} \,. \tag{5}$$

The first contribution, $\mathbf{D}^{\rho\rho} \cdot \nabla \boldsymbol{\rho}$, describes the free diffusion of cells along cell density gradients $\nabla \boldsymbol{\rho}$ and is the continuum consequence of random walk and contact inhibition at the cell level represented through the biological diffusion tensor $\mathbf{D}^{\rho\rho}$. The second contribution, $\mathbf{D}^{\rho\mathrm{c}} \cdot \nabla \mathbf{c}$, characterizes the phenomenon of chemotaxis and is associated with directed diffusion along chemical concentration gradients $\nabla \mathbf{c}$. The chemotactic diffusion tensor $\mathbf{D}^{\rho\mathrm{c}}$ can either be constant or depend on the local chemical concentrations $\mathbf{c}$ and cell densities $\boldsymbol{\rho}$. The biological source consists of a mitotic contribution $\mathbf{f}^{\rho}_{\mathrm{m}}$ and an apoptotic contribution $\mathbf{f}^{\rho}_{\mathrm{a}}$, which typically scales linearly with the cell density $\boldsymbol{\rho}$,

$$\mathbf{f}^{\rho}(\mathbf{c}, \boldsymbol{\rho}, \nabla \boldsymbol{\varphi}) = \mathbf{f}^{\rho}_{\mathrm{m}}(\mathbf{c}, \boldsymbol{\rho}, \nabla \boldsymbol{\varphi}) - \mathbf{f}^{\rho}_{\mathrm{a}}(\mathbf{c}, \boldsymbol{\rho}, \nabla \boldsymbol{\varphi})\, \boldsymbol{\rho} \tag{6}$$

The mitotic and apoptotic terms $\mathbf{f}^{\rho}_{\mathrm{m}}$ and $\mathbf{f}^{\rho}_{\mathrm{a}}$ can be functions of all chemical concentrations $\mathbf{c}$, all cell populations $\boldsymbol{\rho}$, and of mechanical cues $\nabla \boldsymbol{\varphi}$. In homeostasis, in the absence of biological gradients $\nabla \boldsymbol{\rho} = \mathbf{0}$, the mitotic and apoptotic rates balance each other, $\mathbf{f}^{\rho}_{\mathrm{m}} = \mathbf{f}^{\rho}_{\mathrm{a}}\, \boldsymbol{\rho}$.

2.3. Mechanical problem: Mechanical deformation

Mechanically, we assume that the mechanical problem is quasi-static and balances the mechanical flux $\boldsymbol{\sigma}$ with the mechanical source $\boldsymbol{f}^{\varphi}$,

$$\mathbf{0} = \operatorname{div} \boldsymbol{\sigma}\,(\nabla \boldsymbol{\varphi}, \mathbf{n}, \mathbf{w}) + \boldsymbol{f}^{\varphi} \,. \tag{7}$$

The mechanical flux $\boldsymbol{\sigma}$, the Cauchy stress, typically consists of two contributions,

$$\boldsymbol{\sigma} = \boldsymbol{\sigma}^{\mathrm{mat}}(\nabla \boldsymbol{\varphi}) + \mathbf{w}\, \boldsymbol{\sigma}^{\mathrm{fib}}(\nabla \boldsymbol{\varphi}, \mathbf{n}) \,. \tag{8}$$

The first contribution $\boldsymbol{\sigma}^{\mathrm{mat}}$ describes the isotropic water-based matrix as a function of the deformation gradient $\nabla \boldsymbol{\varphi}$. The second contribution $\boldsymbol{\sigma}^{\mathrm{fib}}$ describes the anisotropic response of fibrous constituents such as elastin, collagen, or smooth muscle as a function of the deformation gradient $\nabla \boldsymbol{\varphi}$ and preferred microstructural directions $\mathbf{n}$, scaled by the fiber content $\mathbf{w}$. The mechanical source $\boldsymbol{f}^{\varphi}$, the external mechanical force such as gravity, is typically negligible in the context of inflammation-based systems,

$$\boldsymbol{f}^{\varphi} = \mathbf{0} \,. \tag{9}$$

Biological cells continuously interact with and remodel the tissue in their immediate environment to establish a well defined microstructural arrangement in healthy tissue. After an injury, this microstructure of the healthy skin disappears. Local remodeling by cells becomes the crucial connecting point between the chemical, biological, and mechanical fields [28]. We typically model this coupling through the internal variables $\mathbf{n}$ and $\mathbf{w}$, which evolve in response to cell population dynamics $\boldsymbol{\rho}$. In the most general setting, we allow the microstructural directions $\mathbf{n}$ to gradually reorient according to a set of local evolution equations [12], e.g., driven by chemical gradients $\nabla \mathbf{c}$, by biological gradients $\nabla \boldsymbol{\rho}$, by mechanical gradients $\nabla \boldsymbol{\varphi}$, and by the current microstructural directions $\mathbf{n}$,

$$\dot{\mathbf{n}} = \mathbf{f}^{\mathrm{n}}(\nabla \mathbf{c}, \nabla \boldsymbol{\rho}, \nabla \boldsymbol{\varphi}, \mathbf{n}) \,. \tag{10}$$

Similarly, the local fiber content $\mathbf{w}$ can evolve in time, e.g., driven by chemical concentrations $\mathbf{c}$, by biological cell densities $\boldsymbol{\rho}$, by mechanical gradients $\nabla \boldsymbol{\varphi}$, and by the current fiber content $\mathbf{w}$,

$$\dot{\mathbf{w}} = \mathbf{f}^{\mathrm{w}}(\mathbf{c}, \boldsymbol{\rho}, \nabla \boldsymbol{\varphi}, \mathbf{w}) \,. \tag{11}$$

Even though the microstructural direction $\mathbf{n}$ and the microstructural fiber content $\mathbf{w}$ are parametrized in terms of inhomogeneous fields, their evolution equations are strictly local as they do not contain any gradient or divergence terms. This suggests to treat the microstructural information $\mathbf{n}$ and $\mathbf{w}$ as a set of internal variables [15, 29].

In summary, we represent the chemo-bio-mechanical problem through a system of three sets of partial differential equations for the chemical concentrations $\mathbf{c}$, the biological cell densities $\boldsymbol{\rho}$, and the mechanical deformation $\boldsymbol{\varphi}$, locally supplemented by two sets of ordinary differential equations for the microstructural directions $\mathbf{n}$ and the microstructural fiber content $\mathbf{w}$. In the following section, we will specify these generic equations to explore a particular model problem of wound healing.

3. Model problem of wound healing

In this section, we illustrate the features of the proposed generic framework in terms of a simple model problem of wound healing restricting attention to a few key players. We represent the chemical problem through the concentration of the inflammatory signal $c(\boldsymbol{X}, t)$, the biological problem through the fibroblast density $\rho(\boldsymbol{X}, t)$, and the mechanical problem through the deformation $\boldsymbol{\varphi}(\boldsymbol{X}, t)$ supplemented by the collagen content $w(\boldsymbol{X}, t)$ as local internal variable. We assume that the collagen fiber orientation $\boldsymbol{n}(\boldsymbol{X}, t)$ remains constant throughout the healing process.

3.1. Chemical problem: Inflammatory signal

Chemically, we characterize the response through the inflammatory signal c, which represents the initial recruitment of macrophages and their contribution to generate growth factor attractors for fibroblasts. According to the generic chemical balance law (1), we balance its rate of change with the chemical flux $\boldsymbol{q}^c$ and the chemical source f^c,

$$\dot{c} = \operatorname{div} \boldsymbol{q}^c + f^c \,. \tag{12}$$

For the chemical flux, we assume that the inflammatory signal diffuses freely in space along its own gradient ∇c,

$$\boldsymbol{q}^c = D^{cc} \, \nabla c \,. \tag{13}$$

where D^{cc} is the isotropic chemical diffusion coefficient. For the chemical source, we assume that the inflammatory signal has no production component and displays a linear degradation,

$$f^c = -k \, c \,, \tag{14}$$

where k is the chemical degradation rate.

3.2. Biological problem: Fibroblasts

Biologially, we characterize the response through the fibroblast density ρ. According to the generic biological balance law (4), we balance its rate of change with the biological flux $\boldsymbol{q}^\rho$ and the biological source f^ρ,

$$\dot{\rho} = \operatorname{div} \boldsymbol{q}^\rho + f^\rho \,. \tag{15}$$

For the biological flux, we assume that fibroblasts are motile cells, which diffuse freely along their own gradients $\nabla\rho$ perturbed by a biased diffusion towards the gradient of the inflammatory signal ∇c,

$$\boldsymbol{q}^\rho = D^{\rho\rho} \, \nabla\rho + a \, \rho \, \nabla c \,, \tag{16}$$

where $D^{\rho\rho}$ and $D^{\rho c} = a\,\rho$ denote the isotropic biological and chemotactic diffusion coefficients. For the biological source, we make the following ansatz in terms of the fibroblast density ρ and the intensity of the inflammatory signal c,

$$f^\rho = k_1 \, [\, \rho - \rho_0 \,] + k_2 \, c \, \rho \tag{17}$$

where ρ_0 is the homeostatic fibroblast concentration, k_1 is the physiological mitotic and apoptotic rate, and k_2 is the mitotic rate induced by the inflammatory signal c. Under healthy conditions, fibroblast mitosis and apoptosis balance one another to ensure a stable fibroblast population ρ_0. However, in the presence of inflammatory signals, the mitotic rate increases and creates an imbalance with respect to the steady state ρ_0 to increase the fibroblast density.

3.3. Mechanical problem: Deformation

Mechancially, we characterize the response through the deformation $\boldsymbol{\varphi}$, from which we derive the deformation gradient $\boldsymbol{F} = \nabla\boldsymbol{\varphi}$ and the left Cauchy-Green deformation tensor $\boldsymbol{b} = \boldsymbol{F} \cdot \boldsymbol{F}^{\mathrm{t}}$ as key kinematic variables. According to the mechanical balance law (7), we balance the mechanical flux $\boldsymbol{\sigma}$ characterizing the Cauchy stress and the mechanical source $\boldsymbol{f}^\varphi$ characterizing the external mechanical forces,

$$\boldsymbol{0} = \operatorname{div} \boldsymbol{\sigma} + \boldsymbol{f}^\varphi \,. \tag{18}$$

Skin has a well organized microstructure with an isotropic water-based matrix that serves as a scaffold for the anisotropic collagen network with a preferred orientation $\boldsymbol{n}_0$ [5]. We characterize its constitutive response through a compressible, transversely isotropic, hyperelastic free energy function,

$$\psi = \psi^{\mathrm{mat}}(J, I_1) + w \, \psi^{\mathrm{fib}}(I_1, I_4) \,, \tag{19}$$

which consists of an isotropic part ψ^{mat} for the water-based matrix and an anisotropic part ψ^{fib} for the collagen network weighted by the collagen content w. Here, we have introduced three kinematic invariants, the Jacobian $J = \det \boldsymbol{F}$ for the volumetric response, the first invariant $I_1 = \boldsymbol{b} : \boldsymbol{I}$ for the isotropic response, and the fourth invariant $I_4 = [\boldsymbol{n} \otimes \boldsymbol{n}] : \boldsymbol{I}$ for the anisotropic response, where $\boldsymbol{n} = \boldsymbol{F} \cdot \boldsymbol{n}_0$ is the preferred collagen fiber orientation in the deformed configuration [56]. We model the matrix material as standard isotropic, compressible Neo-Hooke-type parameterized in terms of the Lamé constants λ and μ and the collagen fibers as Holzapfel-type [16], parameterized in terms of the collagen stiffness c_1, the nonlinearity c_2, and the fiber dispersion κ,

$$\begin{aligned} \psi^{\mathrm{mat}} &= \tfrac{1}{2} \, \mu \, [\, I_1 - 3 \,] - \mu \ln J + \tfrac{1}{2} \lambda \, \ln^2 J \\ \psi^{\mathrm{fib}} &= \tfrac{1}{2} \, c_1 / c_2 \, [\, \exp(c_2 \, [\, \kappa I_1 + [\, 1 - 3\kappa \,] \, I_4 - 1]^2) - 1 \,] \,. \end{aligned} \tag{20}$$

The additive decomposition of the strain energy function translates into the additive decomposition of the Cauchy stress according to the generic ansatz (8),

$$\boldsymbol{\sigma} = \boldsymbol{F} \cdot \frac{2}{J} \frac{\partial \psi}{\partial \boldsymbol{C}} \cdot \boldsymbol{F}^{\mathrm{t}} = \boldsymbol{\sigma}^{\mathrm{mat}} + w \cdot \boldsymbol{\sigma}^{\mathrm{fib}} \,, \tag{21}$$

with the following matrix and fiber contributions,

$$\begin{aligned} \boldsymbol{\sigma}^{\mathrm{mat}} &= \boldsymbol{F} \cdot \frac{2}{J} \frac{\partial \psi^{\mathrm{mat}}}{\partial \boldsymbol{C}} \cdot \boldsymbol{F}^{\mathrm{t}} = \mu \, [\, \boldsymbol{b} - \boldsymbol{I} \,] + \lambda \, \ln J \, \boldsymbol{I} \\ \boldsymbol{\sigma}^{\mathrm{fib}} &= \boldsymbol{F} \cdot \frac{2}{J} \frac{\partial \psi^{\mathrm{fib}}}{\partial \boldsymbol{C}} \cdot \boldsymbol{F}^{\mathrm{t}} = 2 \, \psi_1 \, \boldsymbol{b} + 2 \, \psi_4 \, \boldsymbol{n} \otimes \boldsymbol{n} \,. \end{aligned} \tag{22}$$

Here, ψ_1 and ψ_4 denote the first derivatives of the fiber energy with respect to the first and fourth invariants, $\psi_i = \partial \psi^{\mathrm{fib}} \, / \, \partial I_i$,

$$\begin{aligned} \psi_1 &= c_0 + c_1 \kappa \quad [\, \kappa I_1 + [\, 1 - 3\kappa \,] I_4 - 1 \,] \\ &\qquad \exp(c_2 \, [\kappa I_1 + [\, 1 - 3\kappa \,] I_4 - 1 \,]^2) \\ \psi_4 &= c_1 [1 - 3\kappa] \, [\, \kappa I_1 + [\, 1 - 3\kappa \,] I_4 - 1 \,] \\ &\qquad \exp(c_2 \, [\kappa I_1 + [\, 1 - 3\kappa \,] I_4 - 1 \,]^2) \,. \end{aligned} \tag{23}$$

For the mechanical source, we assume that external forces such as gravity do not play a major role during wound healing and can therefore be neglected,

$$\boldsymbol{f}^\varphi = \boldsymbol{0} \,. \tag{24}$$

It remains to characterize the evolution of the collagen content w, which we treat locally as internal variable. We assume that healthy skin possess a homeostatic collagen content w_0. After an injury, the collagen content decreases dramatically in the affected region. It is the task of the fibroblasts to deposit new collagen to restore skin's mechanical properties. We therefore model the evolution of the collagen content $\dot{w}$ to depend on the chemical signal c, the fibroblast density ρ, and the current collagen content w itself, specifically,

$$\dot{w} = f^w \quad \text{with} \quad f^w = \frac{\rho\,\gamma}{1+w^2}\left[\,1 - w + \frac{\alpha\,c\,\gamma}{1+c}\,\right]. \tag{25}$$

Here, γ denotes the physiological collagen deposition rate and α denotes the increase in collagen synthesis in response to inflammation c.

4. Computational modeling of wound healing

To characterize the spatio-temporal evolution of the inflammatory signal c, the fibroblast density ρ, the deformation $\boldsymbol{\varphi}$, and the collagen content w, we solve the global balance equations (12), (15), and (18) along with the local evolution equation (25).

4.1. Strong form

To derive the algorithmic solution we begin by restating the global balance equations (12), (15), and (18) in their residual form in terms of the chemical, biological, and mechanical residuals R^c, R^ϕ, and $\mathbf{R}^\varphi$,

$$\begin{aligned}
\mathsf{R}^c &= \dot{c} - \operatorname{div}\boldsymbol{q}^c - f^c \doteq 0 && \text{in } \mathcal{B}\\
\mathsf{R}^\rho &= \dot{\rho} - \operatorname{div}\boldsymbol{q}^\rho - f^\rho \doteq 0 && \text{in } \mathcal{B}\\
\mathbf{R}^\varphi &= -\operatorname{div}\boldsymbol{\sigma} - \boldsymbol{f}^\varphi \doteq \mathbf{0} && \text{in } \mathcal{B}\,.
\end{aligned} \tag{26}$$

To define the corresponding boundary conditions, we decompose the boundary $\partial\mathcal{B}$ into disjoint parts $\partial\mathcal{B}^c$ and $\partial\mathcal{B}^{qc}$ for the chemical problem, $\partial\mathcal{B}^\phi$ and $\partial\mathcal{B}^{q\rho}$ for the biological problem, and $\partial\mathcal{B}^\varphi$ and $\partial\mathcal{B}^\sigma$ for the mechanical problem. We prescribe Dirichlet boundary conditions $c = c^\mathrm{p}$ on $\partial\mathcal{B}^c$, $\rho = \rho^\mathrm{p}$ on $\partial\mathcal{B}^\rho$, and $\boldsymbol{\varphi} = \boldsymbol{\varphi}^\mathrm{p}$ on $\partial\mathcal{B}^\varphi$, and Neumann boundary conditions $\boldsymbol{q}^c \cdot \boldsymbol{n} = t^c$ on $\partial\mathcal{B}_0^{qc}$, $\boldsymbol{q}^\rho \cdot \boldsymbol{n} = t^\rho$ on $\partial\mathcal{B}_0^{q\rho}$, and $\boldsymbol{\sigma}\cdot\boldsymbol{n} = \boldsymbol{t}^\varphi$ on $\partial\mathcal{B}_0^\sigma$ where $\boldsymbol{n}$ denotes the outward normal to $\partial\mathcal{B}$

4.2. Weak form

To obtain the weak forms of the chemical, biological, and mechanical problems, G^c, G^ρ, and G^φ, we multiply the residual statements (26) and the corresponding Neumann boundary conditions with the scalar- and vector-valued test functions δc, $\delta\rho$ and $\delta\boldsymbol{\varphi}$ and integrate them over the domain $\mathcal{B}$,

$$\begin{aligned}
\mathsf{G}^c &= \int_{\mathcal{B}} \delta c\;\dot{c} + \nabla\delta c\cdot\boldsymbol{q}^c - \delta c\;f^c\,\mathrm{d}v - \int_{\partial\mathcal{B}^{qc}} \delta c\;t^c\,\mathrm{d}a \doteq 0\\
\mathsf{G}^\rho &= \int_{\mathcal{B}} \delta\rho\,\dot{\rho} + \nabla\delta\rho\cdot\boldsymbol{q}^\rho - \delta\rho\;f^\rho\,\mathrm{d}v - \int_{\partial\mathcal{B}^{q\rho}} \delta\rho\;t^\rho\,\mathrm{d}a \doteq 0\\
\mathsf{G}^\varphi &= \int_{\mathcal{B}} \nabla\delta\boldsymbol{\varphi} : \boldsymbol{\sigma} - \delta\boldsymbol{\varphi}\cdot\boldsymbol{f}^\varphi\,\mathrm{d}v - \int_{\partial\mathcal{B}^\sigma} \delta\boldsymbol{\varphi}\cdot\boldsymbol{t}^\varphi\,\mathrm{d}a \doteq 0\,.
\end{aligned} \tag{27}$$

We require that these weak forms vanish identically for all test functions δc, $\delta\rho$, $\delta\boldsymbol{\varphi}$ in $\mathcal{H}_1^0(\mathcal{B})$.

4.3. Discretization in time

To discretize the weak forms (27) in time, we partition the time interval of interest $\mathcal{T}$ into n_{stp} subintervals $[t_n, t]$ as $\mathcal{T} = \bigcup_{n=0}^{n_{step}-1}[t_n, t]$. Here and from now on we omit the subscript $\{\circ\}_{n+1}$ to denote the current time point. We assume, that the primary unknowns c_n, ρ_n and $\boldsymbol{\varphi}_n$ and all derivable quantities are known at the last time point t_n. To advance the unknowns c, ρ, and $\boldsymbol{\varphi}$ to the current time point t, we apply the classical implicit backward Euler time integration scheme and evaluate the governing equations (27) at time t. We apply a finite difference scheme to approximate the first order material time derivatives as

$$\dot{c} = [\,c - c_n\,]\,/\,\Delta t \quad \text{and} \quad \dot{\rho} = [\,\rho - \rho_n\,]\,/\,\Delta t\,, \tag{28}$$

where $\Delta t := t - t_n > 0$ denotes the current time increment.

4.4. Discretization in space

To discretize the weak forms (27) in space, we apply a C^0-continuous interpolation for the inflammatory signal c, the fibroblast density ρ, and the deformation $\boldsymbol{\rho}$, and allow the collagen content w to be C^{-1} continuous. Accordingly, we introduce c, ρ, and $\boldsymbol{\varphi}$ globally on the node point level, and store w locally on the integration point level. We discretize the domain of interest $\mathcal{B}$ into n_{el} elements $\mathcal{B}_e$ as $\mathcal{B} = \bigcup_{e=1}^{n_{el}}\mathcal{B}_e$. We adopt a Bubnov-Galerkin approach and interpolate the trial functions $c^h, \rho^h, \boldsymbol{\varphi}^h$ in $\mathcal{H}_1(\mathcal{B})$ with the same basis function N^c, N^ρ, and N^φ as the test functions δc^h, $\delta\rho^h$, $\delta\boldsymbol{\varphi}^h$ in $\mathcal{H}_1^0(\mathcal{B})$ on the element level,

$$\begin{aligned}
\delta c^h &= \textstyle\sum_{i=1}^{n_{ec}} N_i^c\,\delta c_i \quad & \delta\rho^h &= \textstyle\sum_{j=1}^{n_{e\rho}} N_j^\rho\,\delta\rho_j \quad & \delta\boldsymbol{\varphi}^h &= \textstyle\sum_{k=1}^{n_{e\varphi}} N_k^\varphi\,\delta\boldsymbol{\varphi}_k\\
c^h &= \textstyle\sum_{l=1}^{n_{ec}} N_l^c\;c_l \quad & \rho^h &= \textstyle\sum_{m=1}^{n_{e\rho}} N_m^\rho\,\rho_m \quad & \boldsymbol{\varphi}^h &= \textstyle\sum_{n=1}^{n_{e\varphi}} N_n^\varphi\,\boldsymbol{\varphi}_n\,.
\end{aligned} \tag{29}$$

We adopt the isoparametric concept and interpolate the local element geometry with the same basis functions N^φ as the test and trial functions $\boldsymbol{\varphi}^h$ and $\delta\boldsymbol{\varphi}^h$.

4.5. Discrete algoroithmic residuals

With the discretizations in time (28) and space (29), the weak forms (27) translate into the discrete algorithmic residuals,

$$\begin{aligned}
\mathsf{R}_I^c &= \mathop{\mathbf{A}}_{e=1}^{n_{el}} \int_{\mathcal{B}_e} N_i^c\;\frac{c - c_n}{\Delta t} + \nabla N_i^c\cdot\boldsymbol{q}^c - N_i^c\,f^c\,\mathrm{d}v - \int_{\partial\mathcal{B}_e^{qc}} N_i^c\;t^c\,\mathrm{d}a \doteq 0\\
\mathsf{R}_J^\rho &= \mathop{\mathbf{A}}_{e=1}^{n_{el}} \int_{\mathcal{B}_e} N_j^\rho\;\frac{\rho - \rho_n}{\Delta t} + \nabla N_j^\rho\cdot\boldsymbol{q}^\rho - N_j^\rho\,f^\rho\,\mathrm{d}v - \int_{\partial\mathcal{B}_e^{q\rho}} N_j^\rho\;t^\rho\,\mathrm{d}a \doteq 0\\
\mathbf{R}_K^\varphi &= \mathop{\mathbf{A}}_{e=1}^{n_{el}} \int_{\mathcal{B}_e} \nabla N_k^\varphi\cdot\boldsymbol{\sigma} - N_k^\varphi\,\boldsymbol{f}^\varphi\,\mathrm{d}v - \int_{\partial\mathcal{B}_e^\sigma} N_k^\varphi\;\boldsymbol{t}^\varphi\,\mathrm{d}a \doteq \mathbf{0}\,.
\end{aligned} \tag{30}$$

Here, the operator $\mathbf{A}$ symbolizes the assembly of all element contributions at the element nodes $i = 1, ..., n_{ec}$, $j = 1, ..., n_{e\rho}$, and $k = 1, ..., n_{e\varphi}$ to the overall residuals at the global nodes $I = 1, ..., n_{nc}$, $J = 1, ..., n_{n\rho}$, $K = 1, ..., n_{n\varphi}$.

4.6. Linearization

Although it is possible and sometimes advantageous to solve the discrete residual equations (30) sequentially in a staggered sense, here we discuss the overall solution within a monolithic incremental iterative Newton–Raphson scheme. The Newton–Raphson scheme relies on a consistent algorithmic linearization of the governing equations,

$$\begin{aligned}
\mathsf{R}^c_I &= \mathsf{R}^c_{Ii} + \sum_{L=1}^{n_{nc}} \mathsf{K}^{cc}_{IL}\ \mathrm{d}c_L + \sum_{M=1}^{n_{n\rho}} \mathsf{K}^{c\rho}_{IM}\ \mathrm{d}\rho_M + \sum_{N=1}^{n_{n\varphi}} \mathbf{K}^{c\varphi}_{IN} \cdot \mathrm{d}\boldsymbol{\varphi}_N \doteq 0 \\
\mathsf{R}^\rho_J &= \mathsf{R}^\rho_{Ji} + \sum_{L=1}^{n_{nc}} \mathsf{K}^{\rho c}_{JL}\ \mathrm{d}c_L + \sum_{M=1}^{n_{n\rho}} \mathsf{K}^{\rho\rho}_{JM}\ \mathrm{d}\rho_M + \sum_{N=1}^{n_{n\varphi}} \mathbf{K}^{\rho\varphi}_{JN} \cdot \mathrm{d}\boldsymbol{\varphi}_N \doteq 0 \\
\mathbf{R}^\varphi_K &= \mathbf{R}^\varphi_{Ki} + \sum_{L=1}^{n_{nc}} \mathbf{K}^{\varphi c}_{KL}\ \mathrm{d}c_L + \sum_{M=1}^{n_{n\rho}} \mathbf{K}^{\varphi\rho}_{LM}\ \mathrm{d}\rho_M + \sum_{N=1}^{n_{n\varphi}} \mathbf{K}^{\varphi\varphi}_{KN} \cdot \mathrm{d}\boldsymbol{\varphi}_N \doteq \mathbf{0}\,.
\end{aligned} \tag{31}$$

Here we have introduced the iteration matrices

$$\begin{aligned}
\mathsf{K}^{cc}_{IL} &= \mathop{\mathsf{A}}_{e=1}^{n_{el}} \int_{\mathcal{B}^e} N^c_i\,[\tfrac{1}{\Delta t} - k]\,N^c_l + \nabla N^c_i \cdot D^{cc}\,\nabla N^c_l \,\mathrm{d}V \\
\mathsf{K}^{\rho c}_{JL} &= \mathop{\mathsf{A}}_{e=1}^{n_{el}} \int_{\mathcal{B}^e} N^\rho_j\,[-k_2]\,N^c_l + \nabla N^\rho_j \cdot a\,\rho\,\nabla N^c_l \,\mathrm{d}V \\
\mathsf{K}^{\rho\rho}_{JM} &= \mathop{\mathsf{A}}_{e=1}^{n_{el}} \int_{\mathcal{B}^e} N^\rho_j\,[\tfrac{1}{\Delta t} - k_1 - k_2\,c]\,N^\rho_m + \nabla N^\rho_j \cdot D^{\rho\rho}\,\nabla N^\rho_m \,\mathrm{d}V \\
\mathbf{K}^{\varphi c}_{KL} &= \mathop{\mathsf{A}}_{e=1}^{n_{el}} \int_{\mathcal{B}^e} \nabla N^\varphi_k \cdot \mathrm{d}_c w\,\boldsymbol{\sigma}^{\mathrm{fib}} N^c_l \,\mathrm{d}V \\
\mathbf{K}^{\varphi\rho}_{KM} &= \mathop{\mathsf{A}}_{e=1}^{n_{el}} \int_{\mathcal{B}^e} \nabla N^\varphi_k \cdot \mathrm{d}_\rho w\,\boldsymbol{\sigma}^{\mathrm{fib}} N^\rho_m \,\mathrm{d}V \\
\mathbf{K}^{\varphi\varphi}_{KN} &= \mathop{\mathsf{A}}_{e=1}^{n_{el}} \int_{\mathcal{B}^e} \nabla N^k_\varphi \cdot \mathbb{c} \cdot \nabla N^n_\varphi + \nabla N^k_\varphi \cdot \hat{\boldsymbol{\sigma}} \cdot \nabla N^n_\varphi \,\mathrm{d}V
\end{aligned} \tag{32}$$

with the understanding that, for this special model problem, $\mathbf{K}^{c\rho}_{IM} = \mathbf{0}$, $\mathbf{K}^{c\varphi}_{IN} = \mathbf{0}$, and $\mathbf{K}^{\rho\varphi}_{JN} = \mathbf{0}$. The solution of the system of equations (31) renders the iterative update for the increments of the chemical, biological, and mechanical global unknowns as $\Delta c_I \leftarrow \Delta c_I + \mathrm{d}c_I$ $\Delta\rho_J \leftarrow \Delta\rho_J + \mathrm{d}\rho_J$ and $\Delta\boldsymbol{\varphi}_K \leftarrow \Delta\boldsymbol{\varphi}_K + \mathrm{d}\boldsymbol{\varphi}_K$. It remains to determine the sensitivities of the collagen content $\mathrm{d}_c w$ and $\mathrm{d}_\rho w$ and the Eulerian tangent moduli $\mathbb{c}$ at the constitutive level.

4.7. Algorithmic constitutive equations

On the constitutive level, we first update all internal variables, for our model problem the collagen content w. Then, we determine the chemical, biological, and mechanical fluxes $\boldsymbol{q}^c$, $\boldsymbol{q}^\rho$, and $\boldsymbol{\sigma}$ and sources f^c, f^ρ, and $\boldsymbol{f}^\varphi$, which enter the discrete algorithmic residuals (30). Last, we determine their consistent algorithmic linearizations, for our model problem $\mathrm{d}_c w$ and $\mathrm{d}_\rho w$ and $\mathbb{c}$, which enter the iterations matrices (32). We treat the collagen content w as internal variable and store it locally on the integration point level. To discretize its evolution in time, we apply a finite difference approximation,

$$\dot{w} = [\,w - w_n\,] \,/\, \Delta t\,, \tag{33}$$

combined with an implicit backward Euler time integration scheme. To solve its nonlinear evolution equation, we adopt a local Newton-Raphson scheme. We rephrase the evolution equation (25) in its residual form,

$$\mathsf{R}^w = w - w_n - \frac{\rho\,\gamma}{1+w^2}\left[\,1 - w + \frac{\alpha\,c\,\gamma}{1+c}\,\right]\Delta t \doteq 0 \tag{34}$$

and linearize it consistently as $\mathsf{K}^w = \mathrm{d}_w \mathsf{R}^w$ with

$$\mathsf{K}^w = \frac{\mathrm{d}\mathsf{R}^w}{\mathrm{d}w} = 1 + \frac{\rho\,\gamma}{1+w^2}\left[1 + \frac{2w}{1+w^2}\left[1 - w - \frac{\alpha\,c\,\gamma}{1+c}\right]\right]\Delta t \tag{35}$$

to incrementally update the collagen content $w \leftarrow w - \mathsf{R}^w/\mathsf{K}^w$ on the integration point level. Upon local equilibrium, we determine the fluxes $\boldsymbol{q}^c$, $\boldsymbol{q}^\rho$, and $\boldsymbol{\sigma}$ and sources f^c, f^ρ, and $\boldsymbol{f}^\varphi$ for the global residuals (30). Next, we determine the linearizations $\mathrm{d}_c w = \partial_c \dot{w}\,\Delta t \,/\, \mathsf{K}^w$ with $\partial_c \dot{w}$ from equation (25),

$$\mathrm{d}_c w = \frac{\rho\gamma}{1+w^2}\left[\frac{\alpha\gamma}{1+c} - \frac{\alpha\,c\,\gamma}{[1+c]^2}\right]\Delta t \,/\, \mathsf{K}^w\,, \tag{36}$$

and $\mathrm{d}_\rho w = \partial_\rho \dot{w}\,\Delta t \,/\, \mathsf{K}^w$ with $\partial_\rho \dot{w}$ from equation (25),

$$\mathrm{d}_\rho w = \frac{\gamma}{1+w^2}\left[1 - w + \frac{\alpha\,c\,\gamma}{1+c}\right]\Delta t \,/\, \mathsf{K}^w\,, \tag{37}$$

for the global iterations matrices (32). Last, we determine the Eulerian constitutive moduli $\mathbb{c}$,

$$\mathbb{c} = \mathbb{c}^{\mathrm{mat}} + w \cdot \mathbb{c}^{\mathrm{fib}}\,, \tag{38}$$

with matrix and fiber contributions,

$$\begin{aligned}
\mathbb{c}^{\mathrm{mat}} &= \quad [\,\lambda\,\boldsymbol{I} \otimes \boldsymbol{I} + 2[\,\mu - \lambda \ln J\,]\,\mathbb{i}\,]/J \\
\mathbb{c}^{\mathrm{fib}} &= 4\,[\psi_{11}\boldsymbol{b}\otimes\boldsymbol{b} + 2\psi_{14}[\boldsymbol{b}\otimes\boldsymbol{n}\otimes\boldsymbol{n}]^{\mathrm{sym}} + \psi_{44}\boldsymbol{n}\otimes\boldsymbol{n}\otimes\boldsymbol{n}\otimes\boldsymbol{n}]/J.
\end{aligned} \tag{39}$$

Here, $\mathbb{i}_{ijkl} = \delta_{ik}\delta_{jl}$. ψ_{11}, ψ_{14} and ψ_{44} denote the second derivatives of the fiber energy with respect to the first and fourth invariants, $\psi_{ij} = \partial^2\psi \,/\, \partial I_i \partial I_j$ with

$$\begin{aligned}
\psi_{11} &= c_1[\,1 + 2\,c_2[\,\kappa I_1 + [1-3\kappa]I_4 - 1]] \\
&\qquad \exp(c_2\,[\kappa I_1 + [\,1-3\kappa\,]I_4 - 1\,]^2)\,\kappa^2 \\
\psi_{14} &= c_1[\,1 + 2\,c_2[\,\kappa I_1 + [1-3\kappa]I_4 - 1]] \\
&\qquad \exp(c_2\,[\kappa I_1 + [\,1-3\kappa\,]I_4 - 1\,]^2)\,\kappa\,[1-3\kappa] \\
\psi_{44} &= c_1[\,1 + 2\,c_2[\,\kappa I_1 + [1-3\kappa]I_4 - 1]] \\
&\qquad \exp(c_2\,[\kappa I_1 + [\,1-3\kappa\,]I_4 - 1\,]^2)\,[1-3\kappa]^2\,.
\end{aligned} \tag{40}$$

5. Examples

In this section, we present selected examples to showcase the features of the present formulation in different wound healing scenarios. The first example is a homogeneous setting, in which we explore wound healing across the temporal scales. We monitor the temporal evolution of the chemical, biological, and mechanical variables and systematically probe the constitutive equations for the chemical, biological, and mechanical source terms. The second example is a heterogeneous setting, in which we explore wound healing across the spatio-temporal scales. We monitor the spatio-temporal evolution of the chemical, biological, and mechanical variables and systematically probe the constitutive equations for the chemical, biological, and mechanical flux terms.

5.1. Wound healing across the temporal scales

First, we explore the temporal evolution of the chemical, biological, and mechanical variables, the inflammatory signal c, the fibroblast density ρ, and the collagen content w in a homogeneous setting. This allows us to systematically probe the constitutive equations for the chemical, biological, and mechanical source terms f^c, f^ρ, and f^w defined in equations (14), (17), and (25) and perform sensitivity analyses with respect to the associated material parameters. The homogeneous setting is characterized through the local versions of equations (1), (4), and (7) resulting in the following system of ordinary differential equations,

$$\begin{aligned} \dot{c} &= -\,k\,c \\ \dot{\rho} &= \;\; k_1\,[\,\rho - \rho_0\,] + k_2\,c\,\rho \\ \dot{w} &= \;\; \rho\,\gamma\,[1 - w + [\alpha\,c\,\gamma]/[1 + c]]/[1 + w^2]\,. \end{aligned}$$

In the following, we use normalized variables to facilitate the interpretation of the simulations. We choose the chemical degradation rate to $k = 0.5\,[1/\text{day}]$, the physiological mitotic and apoptotic rate to $k_1 = 0.833\,[1/\text{day}]$, the mitotic rate induced by the inflammatory signal to $k_2 = 0.3\,[1/\text{day}]$, the homeostatic fibroblast concentration to $\rho_0 = 0.5$, the physiological collagen deposition rate to $\gamma = 0.1$, and the inflammation-induced increase in collagen synthesis to $\alpha = 0.5$ [19]. Initially, the wound is defined by a peak inflammatory signal, $c|_{t=0} = 1$, a negligible fibroblast concentration, $\rho|_{t=0} = 0$, and a clot without collagen, $w|_{t=0} = 0$.

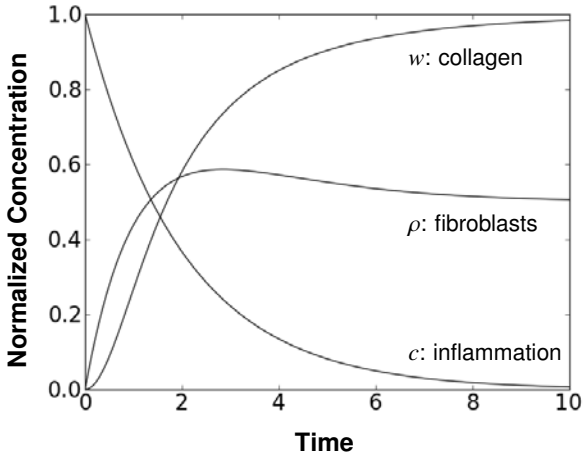

Figure 3: Wound healing across the temporal scales. Temporal evolution of the the inflammatory signal c, the fibroblast density ρ, and the collagen content w.

Figure 3 illustrates the temporal evolution of the chemical, biological, and mechanical variables, the inflammatory signal c, the fibroblast density ρ, and the collagen content w. During the initial phase of wound healing, the inflammatory signal c is significantly elevated. Inflammation induces an increase in the mitotic rate of fibroblasts, which gradually increase in density. At the same time, the chemoattractant decays exponentially towards its baseline value of $c = 0$. The fibroblast density ρ initially overshoots, but then gradually returns to its homeostatic equilibrium value of $\rho = 0.5$. From a structural point of view, the collagen content w is the primary indicator of the healing progress. It increases gradually as the wound recovers. Once the collagen content stabilizes at its physiological value of $w_0 = 1$, the wound is assumed to have healed. Overall, the dynamics of the chemical, biological, and mechanical variables shown in Figure 3 are in qualitative and quantitative agreement with the characteristic features of wound healing.

Next, we perform a systematic sensitivity analysis to explore the impact of the physiological collagen deposition rate γ, the inflammation-induced collagen synthesis rate α, and the inflammation-induced fibroblast mitosis k_2 on the healing process. In all three cases, we monitor the temporal evolution of the collagen content w as the primary mechanical indicator of the healing progress.

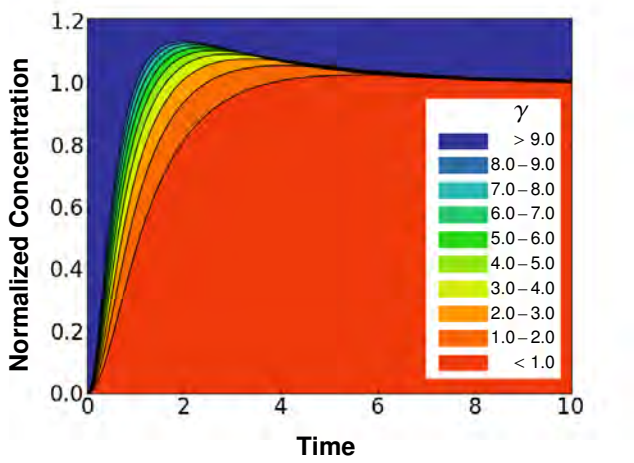

Figure 4: Wound healing across the temporal scales. Sensitivity of collagen content w with respect to collagen deposition rate γ. Increasing the collagen deposition rate induces an overproduction of collagen associated with hypertrophic scarring.

Figure 4 illustrates the sensitivity of the collagen content for varying collagen deposition rates γ. Mathematically, the collagen deposition rate γ directly scales the effects of the fibroblast density ρ on the collagen content w. Biologically, a stronger response by fibroblasts drives an overproduction of collagen, which can be associated with hypertrophic scarring.

Figure 5 illustrates the sensitivity of the collagen content for varying inflammation-induced collagen synthesis rates α. Mathematically, the collagen synthesis rate α directly scales the effects of the inflammatory signal c on the collagen content w. Increasing the influence of the inflammatory signal through α has a similar effect as increasing the collagen deposition rate γ. However, increasing α has a much longer lasting effect, and the collagen content returns to its baseline value much slower. Biologically, a larger influence of the inflammatory signal drives an overproduction of collagen, which can be associated with hypertrophic scarring.

Figure 6 illustrates the sensitivity of the collagen content for varying inflammation-induced mitotic rates k_2. Mathematically, the mitotic rate k_2 increases the fibroblast concentration ρ, which, in turn, increases the collagen content w. Although k_2 does not directly impact the collagen content w, its variation

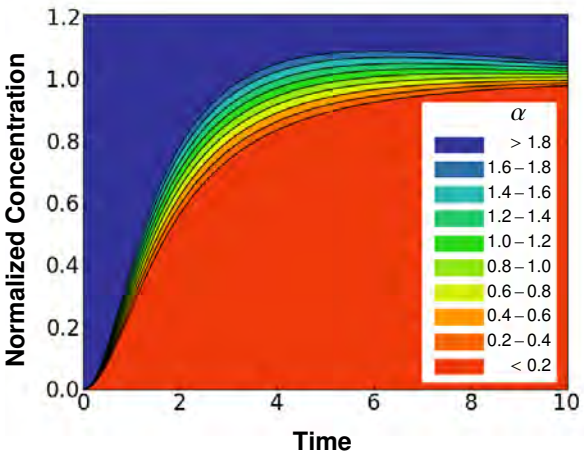

Figure 5: Wound healing across the temporal scales. Sensitivity of collagen content w with respect to inflammation-induced collagen synthesis rate α. Increasing the collagen synthesis rate induces an overproduction of collagen associated with hypertrophic scarring.

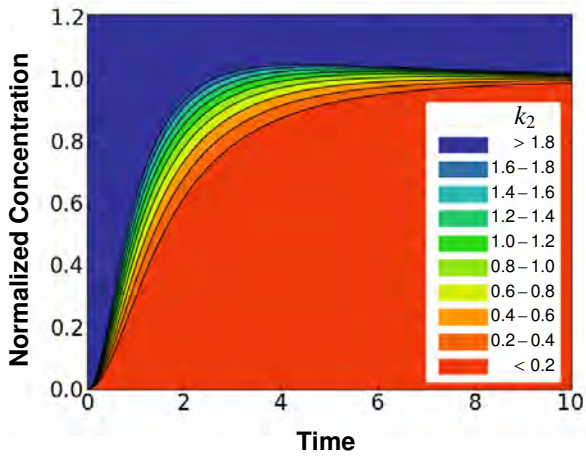

Figure 6: Wound healing across the temporal scales. Sensitivity of collagen content w with respect to inflammation-induced mitotic rate k_2. Increasing the mitotic rate induces an overproduction of collagen associated with hypertrophic scarring.

displays some secondary effects. However, these secondary effects are less pronounced and the collagen concentration remains within normal levels.

This set of homogeneous examples provides confidence that our constitutive equations are indeed able to capture a range of realistic scenarios in wound healing. Nonetheless, the calibration of the model with realistic clinical data remains the next important step.

5.2. Wound healing across the spatio-temporal scales

Now, we explore the spatio-temporal evolution of the chemical, biological, and mechanical variables in a heterogeneous three-dimensional setting. In contrast to the first problem, this now allows us to probe the constitutive equations for the chemical, biological, and mechanical flux terms $\boldsymbol{q}^c$, $\boldsymbol{q}^\rho$ and $\boldsymbol{\sigma}$ defined in equations (13), (16), and (21) and perform sensitivity analyses with respect to the associated material parameters. We idealize the tissue sample as a rectangular prism and model the wound as an elliptical enclosure at its center. The tissue has dimensions of $4\times4\times1\text{cm}^3$. Since the problem has two planes of symmetry, we discretize a quarter of the system using $20\times20\times4 = 1,600$ trilinear brick elements. The boundary conditions are the same for all examples of this subsection. For the chemical and biological problems, we assume homogeneous Neumann boundary conditions. For the mechanics problem, we impose a constant pre-strain of 10% in the x-axis. This boundary condition resembles the pre-stretched state of skin in vivo. In addition, we apply symmetric boundary conditions to reflect the two planes of symmetry.

In addition to the material parameters for the source terms described in detail for the homogeneous problem in Section 5.1, we now need to specify the material parameters for the flux terms. For the chemical problem, the diffusion coefficient is D^{cc} = 0.05 cm/day. For the biological problem, the diffusion coefficient is $D_{\rho\rho}$ = 0.02 cm/day [19]. For the mechanical problem, the Lamé constants are λ = 0.385 MPa and μ = 0.254 MPa, and the Holzapfel parameters are c_1 = 0.15 MPa, c_2 = 0.0418, and κ = 0.05 as calibrated from experiments in pig skin [20]. The collagen fiber orientation is $\boldsymbol{n} = [1,0,0]^{\mathrm{t}}$.

The initial conditions for the chemical, biological, and mechanical fields are heterogeneous, with similar values as in Section 5.1 inside an elliptical wounded region and baseline values outside. We choose the center of the wound at $[x_c, y_c, z_c]$, and parameterize the injured as $[x-x_c]^2/r_x^2 + [y-y_c]^2/r_y^2 < 1$ and $z - z_c < 0.5$. The injured region initially has an elevated inflammatory signal, $c = 1$, and is completely depleted fibroblasts, $\rho = 0$, and collagen, $w = 0$. The healthy tissue outside the wound is free of inflammation, $c = 0$, and has a baseline fibroblasts density, $\rho = \rho_0 = 0.5$, and collagen content, $w = 1$.

Figure 7 shows the spatio-temporal evolution of the inflammatory signal c, the fibroblast density ρ, and the collagen content w for a circular wound with $r_x = r_y = 1$ cm. The last column in Figure 7 summarizes the temporal evolution of the individual fields over the region of the initial injury. The overall behavior is similar to that of the homogeneous wound depicted in Figure 3. The marginal differences between both graphs reflect the influence of the non-wounded surrounding region in the heterogeneous example. These differences disappear over time as the injured region gradually recovers its healthy state. The most distinguishing feature of our framework is the inclusion of common mechanical metrics like stress and strain. Figure 8 displays the spatio-temporal evolution of the Green Lagrange strain E_{xx} in the direction of the collagen fibers. The initial pre-stretch of 10%, applied at the edges of the wound, generates an initially heterogeneous strain distribution. Its spatial profile results from the heterogeneous tissue stiffness introduced through the regionally varying collagen content w. As the healing progresses, the distribution of the strains becomes more and more homogenous as the collagen content gradually returns to its baseline value. The tissue gradually recovers its healthy material properties.

Next, we perform a systematic sensitivity analysis to explore

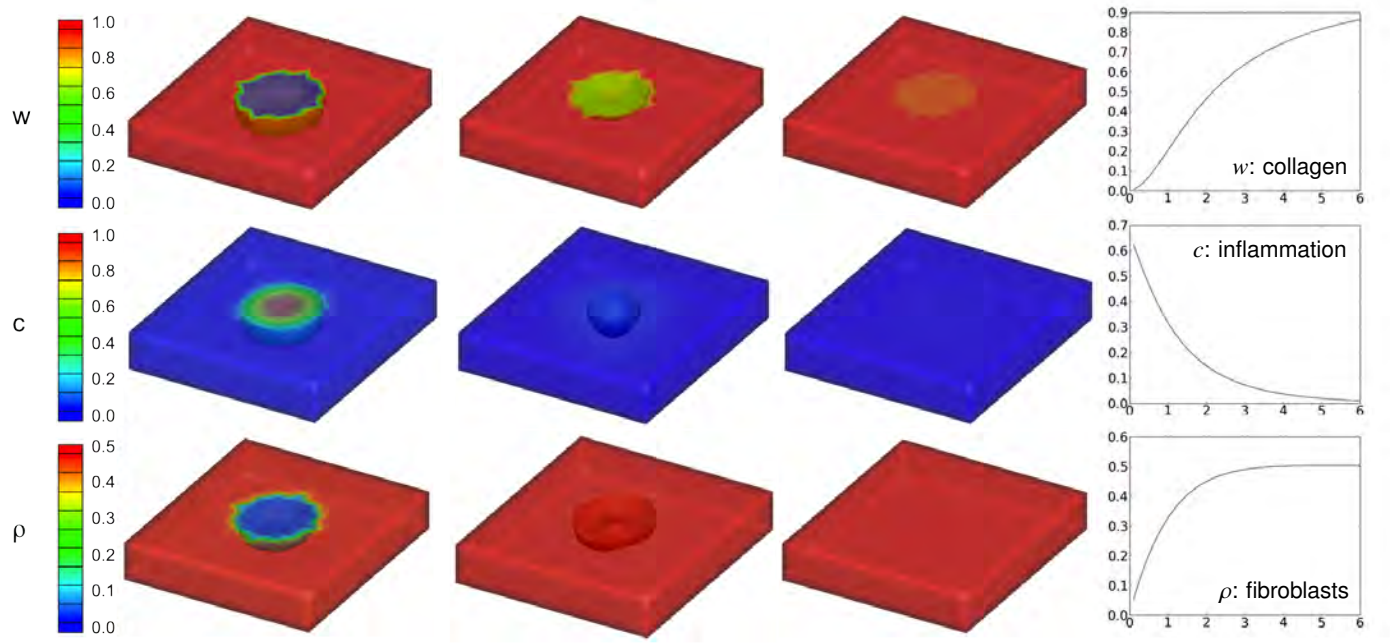

Figure 7: Wound healing across the spatio-temporal scales. Spatio-temporal evolution of the collagen content w, the fibroblast density ρ, and the inflammatory signal c for a circular wound. The last column shows the temporal evolution of the individual fields integrated over the original wound domain. An elevated inflammatory signal c increases the fibroblast density ρ, which results in an increase in the collagen content w.

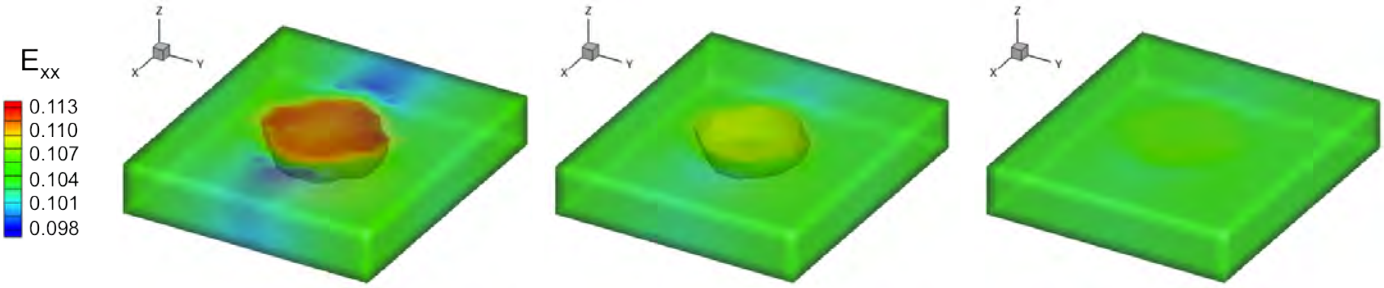

Figure 8: Wound healing across the spatio-temporal scales. Spatio-temporal evolution of the Green Lagrange strain E_{xx} in the direction of the collagen fibers.

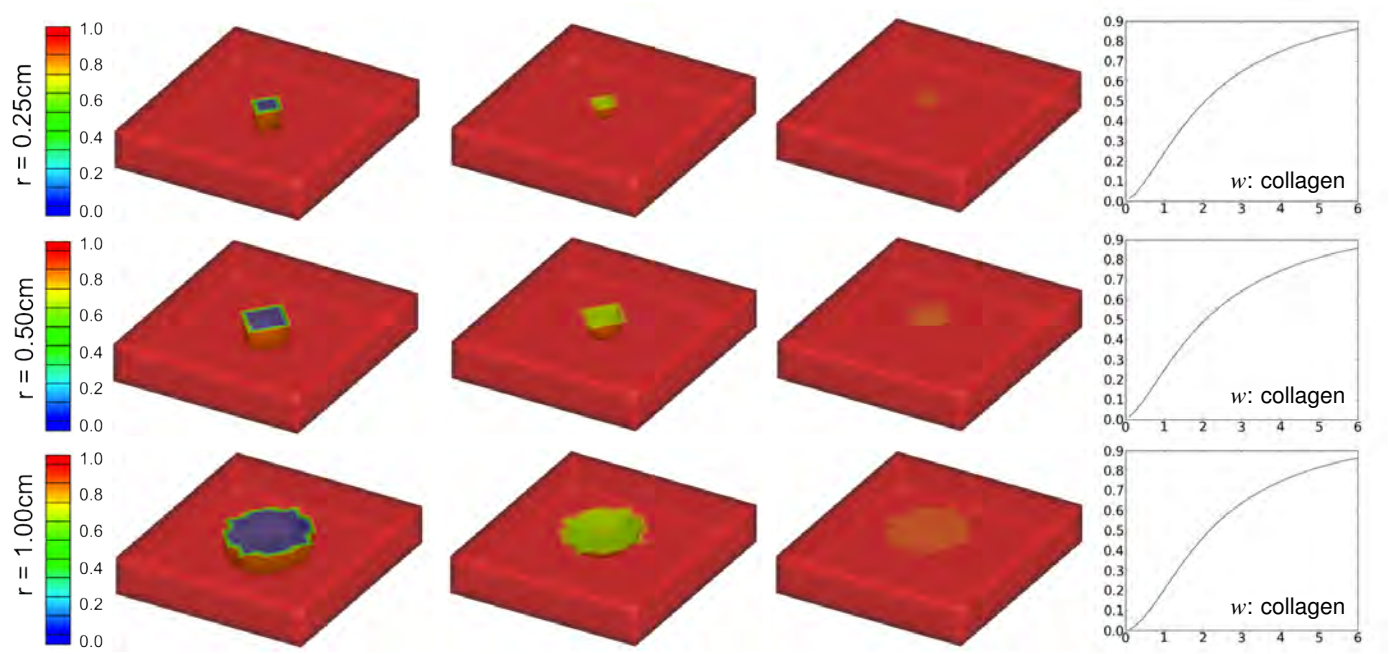

Figure 9: Wound healing across the spatio-temporal scales. Sensitivity of collagen content w with respect to varying wound radii of 0.25 cm, 0.5 cm, and 1.0 cm. The last column shows the temporal evolution of the collagen content integrated over the original wound domain. The time course of the healing process remains unaffected by the wound size. Wound healing is dominated by local source rather than global flux terms, and diffusion plays a minor role.

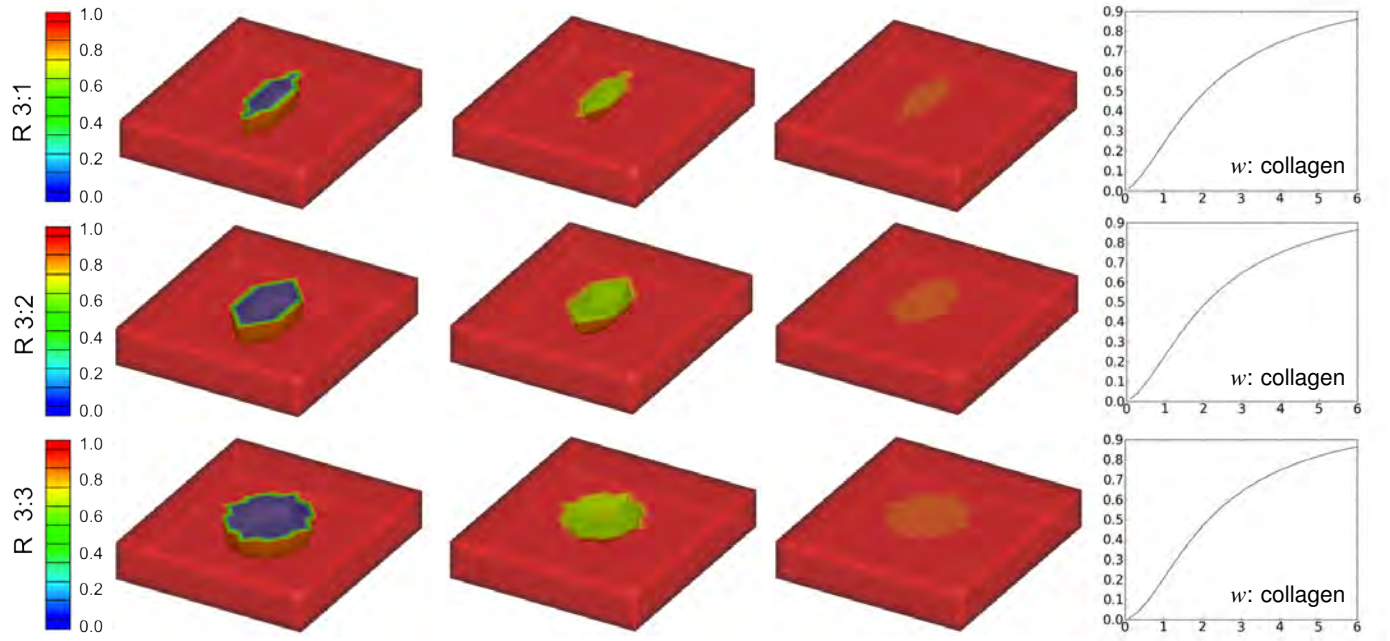

Figure 10: Wound healing across the spatio-temporal scales. Sensitivity of collagen content w with respect to varying elliptical wound shapes with aspect ratios of 1 : 3, 2 : 3, and 3 : 3. The last column shows the temporal evolution of the collagen content integrated over the original wound domain. The time course of the healing process remains unaffected by the wound shape. Wound healing is dominated by local source rather than global flux terms, and diffusion plays a minor role.

the impact of the wound size and the wound shape on the healing process. First, we vary the size of the injured region while maintaining its circular shape. In particular, we study wound radii $r = r_x = r_y$ of 0.25 cm, 0.5 cm, and 1.0 cm. Then, we vary the wound shape and study aspect ratios $r_x : r_y$ of $1 : 3$, $2 : 3$, and $3 : 3$.

Figure 9 displays the spatio-temporal evolution of the collagen content w for varying wound radii of 0.25 cm, 0.5 cm, and 1.0 cm. Unfortunately, the chosen discretization is slightly too coarse to truly capture the circular wound shape, especially for the wound radius of 0.25 cm. However, the basic trends are clearly visible: For the chosen set of material parameters, the time course of the healing process remains unaffected by the wound size. Mathematically, this implies that the evolution equations are dominated by local source rather than global flux terms, and diffusion plays a minor role. Biologically, this implies that, for small wounds, the wound size does not affect the recovery time of the wound as a whole.

Figure 10 displays the spatio-temporal evolution of the collagen content w for varying wound wound shapes with aspect ratios of $1 : 3$, $2 : 3$, and $3 : 3$. Again, the chosen discretization is slightly too coarse to truly capture the elliptical wound shape. Nevertheless, the model captures the basic trends: For the chosen set of material parameters, the time course of the healing process remains unaffected by the wound shape. The integral response is virtually similar to the homogeneous prediction. This is in agreement with the previous simulation of varying wound sizes, for which we had concluded that the evolution equations are dominated by local source rather than global flux terms, and diffusion plays a minor role.

6. Discussion

Hypertrophic scarring is a cutaneous condition characterized by the excessive deposition of collagen, which gives rise to red, thick, stiff, and sometimes painful scar tissue [2]. In physiological wound healing, the production of new collagen and breakdown of old collagen balance one another and the overall collagen content remains constant. In pathological wound healing, however, collagen production dominates collagen breakdown and the overall amount of collagen increases. Fortunately, hypertrophic scars do not extend beyond the initial wounded region, but they may continue to grow for weeks or even months [13]. Mechanics has long been neglected to play a crucial role in scar formation. Yet it is well-known that an increased collagen deposition increases tissue stiffness, and might result in impaired motion when the wound is located close to a joint [50]. Here we have established a novel computational framework for the chemo-bio-mechanics of wound healing to understand the fundamental mechanisms of scar formation. Our novel approach towards simulating wound healing is unconditionally stable, geometrically flexible, and conceptually modular.

Unconditional stability is guaranteed by the use of an implicit backward Euler scheme to discretize the evolution equations in time, both globally and locally. Using implicit time integration schemes is algorithmically robust and allows for larger time steps than explicit schemes. For the solution of the resulting nonlinear system of equations, we suggest an incremental iterative Newton-Raphson scheme, again both globally and locally. While the generic equations of wound healing can be bi-directionally coupled, here we have focused on a uni-directionally coupled model problem. For this specific case, we could have used a sequential solution algorithm. However, for the sake of generality, we have adopted a Newton-Raphson based solution strategy. The conceptual advantage of Newton-Raphson schemes is that they are not only computationally efficient, but they can easily be supplemented by ad hoc time adaptive schemes.

Geometrical flexibility is a crucial novelty of the proposed model. Existing models have mainly been restricted to zero-, one-, and two-dimensional approximations [41]. Our general three-dimensional setting allows us to move forward in the spatial complexity. It is a pivotal step towards the simulation of healing in patient specific geometries. We achieve this flexibility by using a finite element discretization [19]. As opposed to conventional finite volume or finite difference techniques, finite elements, by design, allow for arbitrary geometries [59]. For the first time, we have simulated the healing process in an arbitrary three-dimensional domain. For the sake of illustration, we have used an idealized geometry. The extension to more realistic geometries is, of course, straightforward and part of our current work.

Conceptual modularity allows us to adjust our approach to other existing models [8] or to expand on the particular model proposed here [46, 58]. We have systematically divided the problem of wound healing into three building blocks: chemical, biological, and mechanical [6]. The chemical fields obey a system of partial differential equations common to all reaction-diffusion systems. The biological fields follow a more complex system of partial differential equations that can be specialized for the individual cell populations involved in the healing process. The mechanical fields fall into two categories, global and local, characterized through systems of partial and ordinary differential equations well-established for the continuum mechanics of soft biological tissues. We have highlighted the constitutive coupling between these three different fields for general chemo-bio-mechanical problems. Within this generic setup, we have specified particular constitutive equations to model specific aspects of wound healing [42]. Our approach not only explores relevant healing scenarios for a particular model, but effectively creates a generic framework that can be easily expanded to incorporate other features such as the impact of mechanical cues on cell mitosis or apoptosis [40]. As such, it is not only applicable to explore chemo-bio-mechanical interaction during wound healing in skin, but also in other inflammation-based systems, for example in healing infarcts in cardiac muscle [38].

In addition to these algorithmic aspects, our model accounts for a state-of-the-art mechanical characterization of skin within a continuum mechanics approach [20]. Recently there has been significant development in the theory of the mechanics of living soft collagenous tissues [4, 16, 34]. Unfortunately, these advances have been almost entirely disconnected from recent

trends in systems biology, which have been confined to either rigid geometries or viscoelastic fluids [58]. These simplifications impose great limitations towards understanding the role of mechanical cues during wound healing. A rigorous, accurate mechanical characterization is a fundamental knowledge gap in existing models for wound healing. Here we characterize skin using a hyperelastic strain energy function parametrized in terms of a set of microstructure variables such as collagen orientation [24, 45] and collagen content [39]. By allowing these variables to evolve in time, we establish clear relations between the action of the different cell populations and tissue remodeling. For the first time in the context of wound healing, we can predict finite deformations and impose physiological boundary conditions such as tissue pre-strain [37].

In conclusion, the proposed framework introduces a new generation of wound healing models that may provide fundamental insight into the role of mechanics in scar formation. A unified monolithic finite element treatment of the underlying chemical, biological, and mechanical fields is a first step towards the smooth incorporation of realistic environmental conditions and personalized individual geometries. Our model has the potential to significantly improve effective wound management and optimize treatment options on a patient-specific basis.

Acknowledgements

This work was supported by the Consejo Nacional de Ciencia y Tecnologia CONACyT Fellowship and the Stanford Graduate Fellowship to Adrián Buganza Tepole and by the National Science Foundation CAREER award CMMI-0952021 and INSPIRE award 1233054 and the National Institutes of Health grant U54 GM072970 to Ellen Kuhl.

References

[1] S. Aarabi, K.A. Bhatt, Y. Shi, J. Paterno, E.I. Chang, S.A. Loh, J.W. Holmes, M.T. Longaker, H. Yee, G.C. Gurtner. Mechanical load initiates hypertrophic scar formation through decreased cellular apoptosis. FASEB J. 21 (2007) 32503261.

[2] A. Bayat, D.A. McGrouther, M.W. Ferguson. Skin scarring. BMJ. 326 (2003) 8892.

[3] B.C. Brown, S.P. McKenna, K. Siddhi, D.A. McGrouther, A. Bayat. The hidden cost of skin scars: quality of life after skin scarring. J Plast Reconstr Aesthet Surg. 61 (2008) 10491058.

[4] A. Buganza Tepole, P.C. Ploch, J. Wong, A.K. Gosain, E. Kuhl. Growing skin - A computational model for skin expansion in reconstructive surgery. J Mech Phys Solids. 59 (2011) 2177-2190.

[5] A. Buganza Tepole, A.K. Gosain, E. Kuhl. Stretching skin - The physiological limit and beyond. Int J Nonlin Mech. 47 (2012) 938-949.

[6] A. Buganza Tepole, E. Kuhl. Review: Systems-based approaches towards wound healing. Pediatric Res. 73 (2013) 553-563.

[7] M. Chiquet, L. Gelman, R. Lutz, S. Maier. From mechanotransduction to extracellular matrix gene expression in fibroblasts. Biochim Biophys Acta. 1793 (2009) 911920.

[8] B.D. Cumming, D.L.S. McElwain, Z. Upton. A mathematical model of wound healing and subsequent scarring. J Royal Soc Interface. 7 (2009) 19-34.

[9] J.C. Dallon, J.A. Sherratt, P.K. Maini. Modeling the effects of transforming growth factor-beta on extracellular matrix alignment in dermal wound repair. Wound Repair Regen. 9 (2001) 278286.

[10] R.F. Diegelmann, M.C. Evans. Wound healing: an overview of acute, fibrotic and delayed healing. Front Biosci. 9 (2004) 283289.

[11] C. Flynn, A. Taberner, P. Nielsen. Mechanical characterisation of in vivo human skin using a 3D force-sensitive micro-robot and finite element analysis. Biomech Model Mechanobiol. 10 (2011) 2738.

[12] K. Garikipati, J.E. Olberding, H. Narayanan, E.M. Arruda, K. Grosh, S. Calve. Biological remodeling: Stationary energy, configurational change, internal variables and dissipation. J Mech Phys Solids. 54 (2006) 1493-1515.

[13] G.C. Gurtner, S. Werner, Y. Barrandon, M.T. Longaker. Wound repair and regeneration. Nature. 453 (2008) 314321.

[14] S.P. Herbert, D.Y. Stainier. Molecular control of endothelial cell behaviour during blood vessel morphogenesis. Nat Rev Mol Cell Biol. 12 (2011) 551564.

[15] G. Himpel, A. Menzel, E. Kuhl, P. Steinmann. Time-dependent fiber reorientation of transversely isotropic continua - Finite element formulation and consistent linearization. Int J Num Meth Eng. 73 (2008) 1413-1433.

[16] G.A. Holzapfel, T.C. Gasser, R.W. Ogden. A new constitutive framework for anterial wall mechanics and a comparative study of material models. J Elast. 61 (2000) 1-48.

[17] P.J. Hunter, T.K. Borg. Integration from proteins to organs: the Physiome Project. Nat Rev Mol Cell Biol. 4 (2003) 237243.

[18] E. Javierre, F.J. Vermolen, C. Vuik, S. Zwaag. A mathematical analysis of physiological and morphological aspects of wound closure. J Math Biol. 59 (2009) 605-630.

[19] E. Javierre, P. Moreno, M. Doblare, J.M. Garcia-Aznar. Numerical modeling of a mechano-chemical theory for wound contraction analysis. Int J Solids Struct. 46 (2009) 3597-3606.

[20] J.W.Y. Jor, M.P. Nash, P.M.F. Nielsen, P.J. Hunter. Estimating material parameters of a structurally based constitutive relation for skin mechanics. Biomech Mod Mechanobio. 10 (2011) 767-778.

[21] H. Kitano. Computational systems biology. Nature. 420 (2002) 206210.

[22] E. Kuhl, P. Steinmann. Material forces in open system mechanics. Comp Meth Appl Mech Eng. 193 (2004) 2357-2381.

[23] E. Kuhl, P. Steinmann. Computational modeling of healing - An application of the material force method. Biomech Mod Mechanobio. 2 (2004) 187-203.

[24] E. Kuhl, G.A. Holzapfel. A continuum model for remodeling in living structures. J Mat Sci. 42 (2007) 8811-8823.

[25] Y. Lanir. Constitutive equations for fibrous connective tissues. J Biomech. 16 (1983) 112.

[26] P.K. Maini, D.L. McElwain, D.I. Leavesley. Traveling wave model to interpret a wound-healing cell migration assay for human peritoneal mesothelial cells. Tissue Eng. 10 (2004) 475482.

[27] P. Martin. Wound healingaiming for perfect skin regeneration. Science. 276 (1997) 7581.

[28] S. McDougall, J. Dallon, J. Sherratt, P. Maini. Fibroblast migration and collagen deposition during dermal wound healing: mathematical modelling and clinical implications. Philos Transact A Math Phys Eng Sci. 364 (2006) 13851405.

[29] A. Menzel. A fibre reorientation model for orthotropic multiplicative growth. Biomech Model Mechanobio. 6 (2007) 303320.

[30] S.E. Mutsaers, J.E. Bishop, G. McGrouther, G.J. Laurent. Mechanisms of tissue repair: from wound healing to fibrosis. Int J Biochem Cell Biol. 29 (1997) 517.

[31] H. Narayanan, S.N. Verner, K.L. Mills, R. Kemkemer, K. Garikipati. In silica estimates of the free energy rates in growing tumor spheroids. J Phys Cond Matter. 22 (2010) 194122.

[32] O.O. Olutoye, X. Zhu, D.L. Cass, C.W. Smith. Neutrophil recruitment by fetal porcine endothelial cells: implications in scarless fetal wound healing. Pediatr Res. 58 (2005) 12901294.

[33] J. Paterno, I.N. Vial, V.W. Wong, K.C. Rustad, M. Sorkin, Y. Shi, K.A. Bhatt, H. Thangarajah, J.P. Glotzbach, G.C. Gurtner. Akt-mediated mechanotransduction in murine fibroblasts during hypertrophic scar formation. Wound Repair Regen. 19 (2011) 4958.

[34] E. Pena, M.A. Martinez, B. Calvo, M. Doblare. Application of the natural element method to finite deformation inelastic problems in isotropic and fiber-reinforced biological soft tissues. Comp Meth Appl Mech Eng. 197 (2008) 19831996.

[35] G.J. Pettet, H.M. Byrne, D.L. McElwain, J. Norbury. A model of wound-healing angiogenesis in soft tissue. Math Biosci. 136 (1996) 35-63.

[36] A.A. Qutub, F. Mac Gabhann, E.D. Karagiannis, P. Vempati, A.S. Popel. Multiscale models of angiogenesis. IEEE Eng Med Biol Mag. 28 (2009)

1431.
[37] M.K. Rausch, E. Kuhl. On the effect of prestrain and residual stress in thin biological membranes. J Mech Phys Solids. (2013) doi:10.1016/j.jmps.2013.04.005.
[38] A.D. Rouillard, J.W. Holmes. Mechanical regulation of fibroblast migration and collagen remodeling in healing myocardial infarcts. J Phyisol. 590 (2012) 4585-4602.
[39] P. Saez, E. Pena, M.A. Martinez, E. Kuhl. Mathematical modeling of collagen turnover in biological tissue. J Math Bio. (2013) doi:10.1007/s00285-012-0613-y.
[40] S. Scheiner, P. Pivonka, C. Hellmich. Coupling systems biology with multiscale mechanics, for computer simulations of bone remodeling. Comp Meth Appl Mech Eng. 254 (2013) 181-196.
[41] R.C. Schugart, A. Friedman, R. Zhao, C.K. Sen. Wound angiogenesis as a function of tissue oxygen tension: A mathematical model. Proc Nat Acad Sci. 105 (2008) 2628-2633.
[42] J.A. Sherratt, J.D. Murray. Models of epidermal wound healing. Proc Royal Soc B Bio Sci. 241 (1990) 29-36.
[43] C.L. Simpson, D.M. Patel, K.J. Green. Deconstructing the skin: cytoarchitectural determinants of epidermal morphogenesis. Nat Rev Mol Cell Biol. 12 (2011) 565580.
[44] J. Southern, J. Pitt-Francis, J. Whiteley, D. Stokeley, H. Kobashi, R. Nobes, Y. Kadooka, D. Gavaghan. Multi-scale computational modelling in biology and physiology. Prog Biophys Mol Biol. 96 (2008) 6089.
[45] T. Stylianopoulos, V.H. Barocas. Volume-averaging theory for the stuy of the mechanics of collagen networks. Comp Meth Appl Mech Eng. 196 (2007) 2981-2990.
[46] T. Sun, S. Adra, R. Smallwood, M. Holcombe, S. MacNeil. Exploring hypotheses of the actions of TGF-beta1 in epidermal wound healing using a 3D computational multiscale model of the human epidermis. PLoS ONE. 4 (2009) e8515.
[47] P. Tong, Y.C. Fung. The stress-strain relationship for the skin. J Biomech. 9 (1976) 649657.
[48] R.T. Tranquillo. Stochastic model of leukocyte chemosensory movement. J Math Biol. 25 (1987) 229-262.
[49] R.T. Tranquillo, J.D. Murray. Continuum model of fibroblast-driven wound contraction: Inflammation-mediation. Biomech Model Mechanobiol. 158 (2007) 361-371.
[50] P.D.H.M. Verhaegen, P.P.M. van Zuijlen, N.M. Pennings, J. van Marle, F.B. Niessen, C.M.A.M. van der Horst, E. Middelkoop. Differences in collagen architecture between keloid, hypertrophic scar, normotrophic scar, and normal skin: an objective histopathological analysis. Wound Repair Regen. 17 (2009) 649656.
[51] F.J. Vermolen, E. Javierre. Computer simulations from a finite-element model for wound contraction and closure. J Tissue Viabil. 19 (2010) 43-53.
[52] T. Velnar, T. Bailey, V. Smrkolj. The wound healing process: an overview of the cellular and molecular mechanisms. J Int Med Res. 37 (2009) 15281542.
[53] Y. Vodovotz, M. Csete, J. Bartels, S. Chang, G. An. Translational systems biology of inflammation. PLoS Comput Biol. 4 (2008) e1000014.
[54] Y. Vodovotz. Translational systems biology of inflammation and healing. Wound Repair Regen. 18 (2010) 37.
[55] V.W. Wong, S. Akaishi, M.T. Longaker, G.C. Gurtner. Pushing back: wound mechanotransduction in repair and regeneration. J Invest Dermatol. 131 (2011) 21862196.
[56] J.A. Weiss, B.N. Maker, S. Govindjee. Finite element implementation of incompressible, transversely isotropic hyperelasticity. Comp Meth Appl Mech Eng. 135 (1996) 107128.
[57] V.W. Wong, K. Levi, S. Akaishi, G. Schultz, R.H. Dauskardt. Scar zones: regionspecific differences in skin tension may determine incisional scar formation. Plast Reconstr Surg. 129 (2012) 12721276.
[58] C. Xue, A. Friedman, C.K. Sen. A mathematical model of ischemic cutaneous wounds. Proc Natl Acad Sci. 106 (2009) 1678216787.
[59] A.M. Zöllner, A. Buganza Tepole, A.K. Gosain, E. Kuhl. Growing skin - Tissue expansion in pediatric forehead reconstruction. Biomech Mod Mechanobio. 11 (2012) 855-867.
[60] A.M. Zöllner, A. Buganza Tepole, E. Kuhl. On the biomechanics and mechanobiology of growing skin. J Theor Bio. 297 (2012) 166-175.